Charge-acquired Pb^{2+} boosts actively and selectively electrochemical carbon dioxide reduction reaction to formate

Ningce Zhang [a], Daohao Li [a,*], Xiaoxia Wang [a], Rongsheng Cai [b], Chung-Li Dong [c], Ta Thi Thuy Nga [c], Lijie Zhang [a], Dongjiang Yang [a,*]

[a] *State Key Laboratory of Bio-fibers and Eco-textiles, School of Environmental Science and Engineering, College of Materials Science and Engineering, Qingdao University, Qingdao 266071, PR China*
[b] *Department of Materials, University of Manchester, Manchester M13 9PL, United Kingdom*
[c] *Department of Physics, Tamkang University, New Taipei City 25137, Taiwan*

ARTICLE INFO

ABSTRACT

For lead carbonate-based ($PbCO_3$) carbon dioxide reduction reaction (CO_2RR) electrocatalysts, the electron-deficiency of Pb^{2+} active sites adverse to activate *CO_2 and generate HCOO* intermediates hinder the active and selective CO_2RR to formate. In this work, the Co modified (heterojunction and doping) $PbCO_3$ electrocatalyst is constructed with prominent catalytic activity and high formate selectivity (Faradaic efficiency about 98.15% at −0.70 V vs. RHE). The in-depth experimental and theoretical analyses reveal that the Co-$PbCO_3$ interaction can enable the electron of Co transfer to Pb^{2+}, leading to the charge-acquired Pb^{2+} (CA-Pb^{2+}). Its highly catalytic activity and selectivity of formate is attributed to the reduced formation energy barrier and enhanced adsorption behavior of HCOO* intermediate. The in-situ attenuated total reflection surface-enhanced infrared absorption spectroscopy demonstrates HCOO* intermediate is more likely to generate and adsorb on CA-Pb^{2+} than Pb^{2+}, verifying the charge acquisition of Pb^{2+} enhances the activity and selectivity of formate product.

1. Introduction

Electrocatalytic CO_2 reduction reaction (CO_2RR) is a sustainable strategy to convert CO_2 into worthwhile chemical raw materials and indispensable fuels, such as CO, CH_4, formate, etc. [1–3] Among them, formate is a significant industrial raw material for tanning and food additives, and also has been regarded as ideal candidate for hydrogen storage and fuel cells [4,5]. The key of CO_2RR technology for synthesizing fromate is development of highly active, selective and stable electrocatalysts.

In the CO_2RR pathway, the high activity and selectivity of electrocatalysts for formate product is triggered by two factors: 1) low reaction energy barrier of the catalytic *CO_2 initiation and HCOO* intermediates formation [6,7]; 2) preferential adsorption for HCOO* as compared to *COOH and H* to inhibit the formation of CO, multi-carbon products and H_2 [8,9]. Metal-lead (Pb) has been deemed to be promising electrocatalyst for CO_2RR to formate due to their high H_2 overpotential and facile adsorption of HCOO* intermediates [10–13]. Nevertheless, the high CO_2 conversion selectivity of metal-Pb in actual operation is still

the challenges due to the formation and adsorption of competitive *COOH intermediates during CO_2RR [14–16]. The hetero-metal regulation (alloying or metal-doping) can regulate the electronic structures of electrocatalyst to enhance the CO_2RR performance [17,18]. Nowadays, studies employing bimetal Pb-based materials, such as PbSn [14, 19,20] and PbCu [21,22], illustrated the enhanced formate product, restraining the competing *COOH→*CO route. However, Pb active sites usually suffer from the problem of unstable valence state due to its oxidation (Pb→Pb^{2+}) in operative electrolyte and the simultaneous self-reduction (Pb^{2+}→Pb) during CO_2RR process [23,24]. Thus, the true electronic structure of regulated Pb active site, which delivers low energy barrier of HCOO* formation and preferential HCOO* adsorption, is uncertain. This results in the ambiguous reaction mechanism. Recently, the Pb^{2+} in lead carbonate-based material was redefined as the stably active species for CO_2RR to formate process by Shi et al. [10] However, the high HCOO* formation energy barrier of Pb^{2+} sites still restricts the main rate and selectivity-limiting step of the reaction, [10,11] resulting in inferior catalytic performance. This may be ascribed to the fact that the deficiency of outer orbital electrons of multivalent metal ions

---

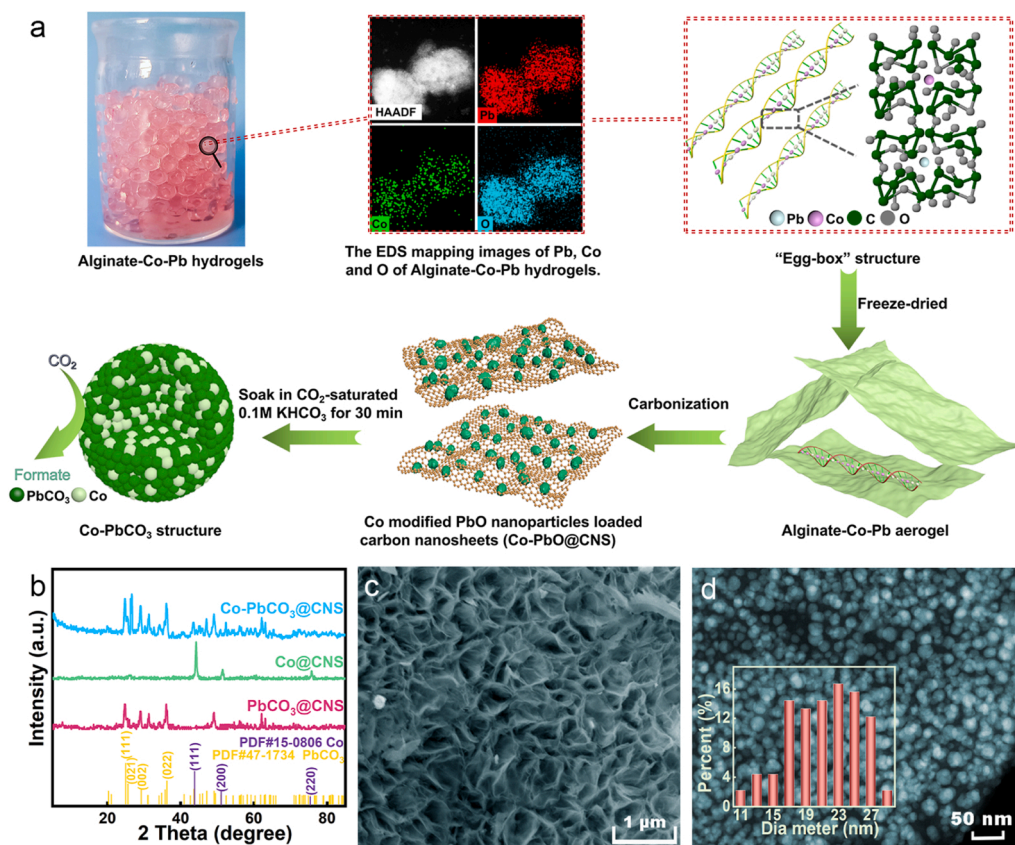**Fig. 1.** (a) Schematic illustration of the synthesis process of Co-PbCO$_3$ @CNS. (b) XRD patterns of Co-PbCO$_3$ @CNS Co@CNS and PbCO$_3$ @CNS. (c) SEM image of Co-PbCO$_3$ @CNS. (d) AC HAADF-STEM image and particle size distribution of Co-PbCO$_3$ @CNS.

seriously affects the delocalized electron, which adverse to activate *CO$_2$, further hindering the *CO$_2$→HCOO* conversion [25,26]. Apparently, the electron-deficient Pb^{2+} sties in stable lead carbonate-based electrocatalyst need to be regulated with supplementary electrons structure to activate *CO$_2$ and drive HCOO* formation.

In this work, the Co modified (heterojunction and doping) PbCO$_3$ nanoparticles loaded carbon nanosheets (Co-PbCO$_3$ @CNS) was synthesized, and both experimental and density functional theory (DFT) calculation results illustrate that the Co-Pb^{2+} interaction enables the electron of Co transfer to Pb^{2+}, that is, the charge-acquired Pb^{2+} (CA-Pb^{2+}). Compared with pure PbCO$_3$ @CNS, the Co-PbCO$_3$ @CNS exhibits superior catalytic activity and selectivity for CO$_2$RR to formate with Faradaic efficiency (FE) of formate (FE$_{formate}$) about 98.15% and a formate partial current density of 9.65 mA cm^{-2} at − 0.70 V vs. RHE. After continuous CO$_2$RR for 20 h, the Co-PbCO$_3$ @CNS is almost no degradation of selectivity, and maintain a stable structure. The in-situ attenuated total reflection surface-enhanced infrared absorption spectroscopy (ATR-SEIRAS) spectroscopy indicates the HCOO* intermediates are more likely to generate and adsorb on CA-Pb^{2+} sites than Pb^{2+}. Moreover, the DFT calculations further demonstrate the electron-rich CA-Pb^{2+} site induces the reduced formation energy barrier and enhanced adsorption behavior of crucial HCOO* intermediate, endowing the high acivity and selectivity of formate product.

2. Experimental

2.1. Synthesis of Co-PbCO$_3$@CNS

The 2 g SA was dissolved in 200 mL distilled water, ufficiently stirred at room temperature to form a uniform 1 wt% SA solution. Subsequently, the above SA solution was added to a mixed Co^{2+}/Pb^{2+} ions

aqueous solution (Co^{2+} 0.1 mol L^{-1} and Pb^{2+} 0.2 mol L^{-1}) by syringe needle to form a spheroidized alginate Co-Pb hydrogels. After soaking for 4 h, filtered and washed the hydrogels, Then the as-prepared alginate Pb-Co hydrogelss were frozen with liquid nitrogen, and dried in the − 80 °C for 48 h via frozen dryer to obtain alginate-Co-Pb aerogels. The obtained alginate-Co-Pb aerogels were annealed at 700 °C for 2 h at a ramp rate of 2 °C min^{-1} under argon. After the reaction was complete, Co-PbO@CNS were obtained. The samples were washed with Acetic acid under ultrasonic conditions for 3 h to remove the excess impurities. Then, washed with distilled water until the PH close to 7 and dried at 60 °C for 12 h. Lastly, soaking the Co-PbO@CNS in the CO$_2$-saturated 0.1 M KHCO$_3$ solution for 30 min, the Co-PbCO$_3$ @CNS was obtained.

2.2. Synthesis of Co@CNS

The above 1 wt% SA solution was added to a 0.1 mol L^{-1} Co^{2+} ions aqueous solutionby syringe needle to form a spheroidized alginate Co hydrogel. After soaking for 4 h, filtered and washed the hydrogels, Then the as-prepared alginate Co hydrogelss were frozen with liquid nitrogen, and dried in the − 80 °C for 48 h via frozen dryer to obtain alginate-Co aerogels. The obtained alginate-Co aerogels were annealed at 700 °C for 2 h at a ramp rate of 2 °C min^{-1} under hydrogen and argon mixed atmosphere. After the reaction was complete, Co@CNS were obtained. The samples were washed with Acetic acid under ultrasonic conditions for 3 h to remove the excess impurities. Then, washed with distilled water until the PH close to 7 and dried at 60 °C for 12 h. Lastly, soaking the Co@CNS in the CO$_2$-saturated 0.1 M KHCO$_3$ solution for 30 min, the Co@CNS was obtained.
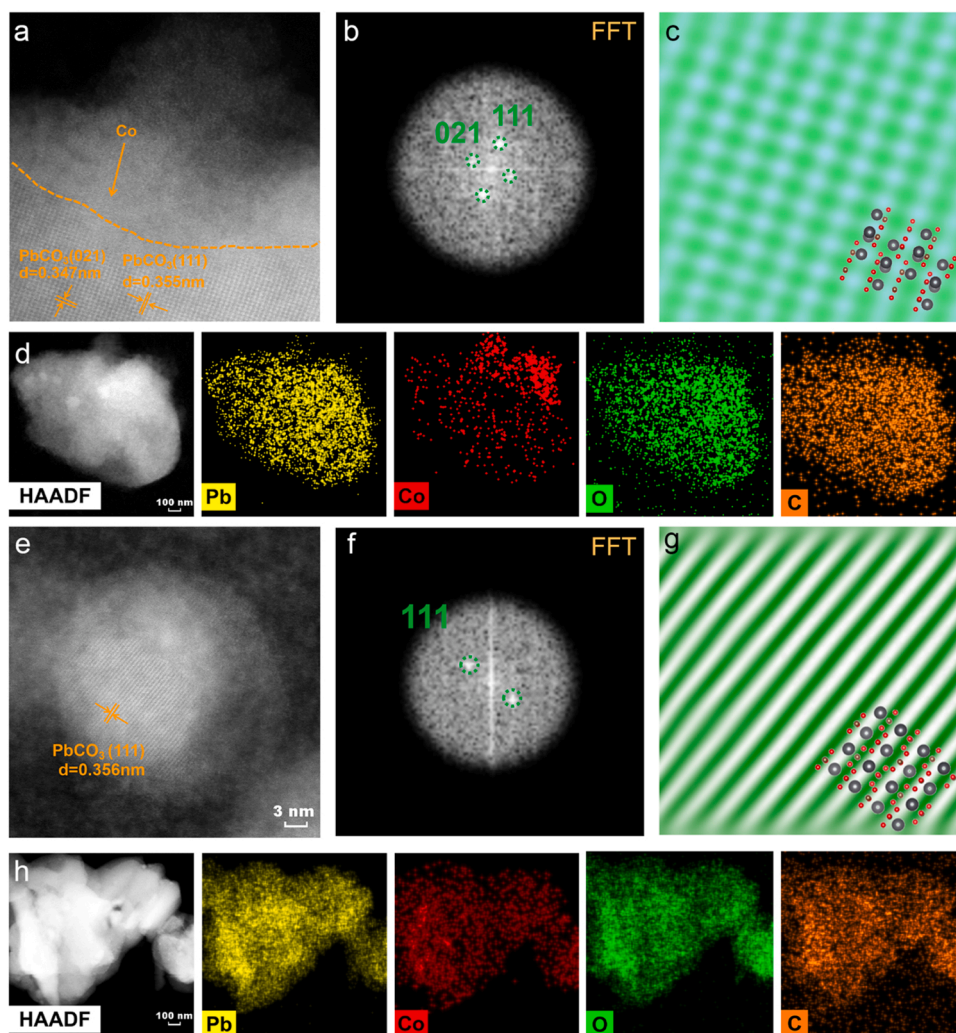
Fig. 2. (a, d) High-magnification AC HAADF-STEM images and intensity profile analysis of Co-PbCO$_3$ @CNS, and the corresponding FFT image of Co-PbCO$_3$ @CNS. (b, e) Inverse FFT and 3D crystal structure of PbCO$_3$. (c, f) The HAADF-STEM and EDS mapping images for Pb, Co and O of Co-PbCO$_3$ @CNS.

2.3. Synthesis of PbCO$_3$@CNS

The above 1 wt% SA solution was added to a 0.1 mol L^{-1} Pb^{2+} ions aqueous solutionby syringe needle to form a spheroidized alginate Pb hydrogels. After soaking for 4 h, filtered and washed the hydrogels, Then the as-prepared alginate Pb hydrogelss were frozen with liquid nitrogen, and dried in the − 80 °C for 48 h via frozen dryer to obtain alginate-Pb aerogels. The obtained alginate-Pb aerogels were annealed at 700 °C for 2 h at a ramp rate of 2 °C min^{-1} under argon. After the reaction was complete, PbO@CNS were obtained. The samples were washed with Acetic acid under ultrasonic conditions for 3 h to remove the excess impurities. Then, washed with distilled water until the PH close to 7 and dried at 60 °C for 12 h. Lastly, soaking the PbO@CNS in the CO$_2$-saturated 0.1 M KHCO$_3$ solution for 30 min, the PbCO$_3$ @CNS was obtained.

3. Results and discussion

3.1. Preparation and characterization of Co-PbCO$_3$@CNS

The preparation process of Co-PbCO$_3$ @CNS is shown in Fig. 1a. The Co-PbO@CNS was firstly synthesized through an ice-templating method [27,28]. 1.0 wt% sodium alginate (SA) solution was added into an aqueous solution of mixed Co^{2+} and Pb^{2+} ions to obtain crosslinked alginate-Co-Pb hydrogels. The energy-dispersive spectroscopy (EDS) mapping images show that the distribution of Co^{2+} and Pb^{2+} is uniform over the entire architecture. Then, the as-prepared alginate-Co-Pb hydrogels were dehydrated via a freeze-drying procedure to generate alginate-Co-Pb aerogels, and the Co-PbO@CNS was obtained after pyrolysis. The alginates macromoleculars were turned into a carbon skeleton, and the chelated Pb^{2+} and Co^{2+} in the "egg-box" structures were transformed to Co-PbO. Lastly, soaking the Co-PbO@CNS in the CO$_2$-saturated 0.1 M KHCO$_3$ solution for 30 min, the Co-PbCO$_3$ @CNS was obtained. The pure PbCO$_3$ @CNS and Co@CNS as contrast samples were also synthesized by the similar process (see Fig. S1-S2 in Supporting Information).

The structures of synthesized samples are firstly confirmed by X-ray diffraction (XRD) measurements. The diffraction peaks at 44.2°, 51.5° and 75.9 are consistent with the (111), (200) and (220) planes of Co (JCPDS no. 15–0860), while the peaks locate at 24.5°, 25.4°, 29.0° and 36.0° etc. are indexed to the (111), (021), (002) and (022) planes of PbCO$_3$ (JCPDS no. 47–1734), respectively (Fig. 1b), implying the successful synthesis of Co-PbCO$_3$ @CNS, PbCO$_3$ @CNS and Co@CNS. The Co K-edge region of the X-ray absorption near-edge structure (XANES) spectrum of Co-PbCO$_3$ @CNS closes to the reference of Co foil (0), implying the presence of Co (Fig. S3). The scanning electron microscopy (SEM) images of Co-PbCO$_3$ @CNS show typical nanosheet morphology (Fig. 1c and S4), which provides sufficiently exposed active sites. The aberration-corrected high angle annular dark-field scanning transmission electron microscopy (AC HAADF-STEM) image proves the evenly distributed and erratically shaped nanoparticles with an average
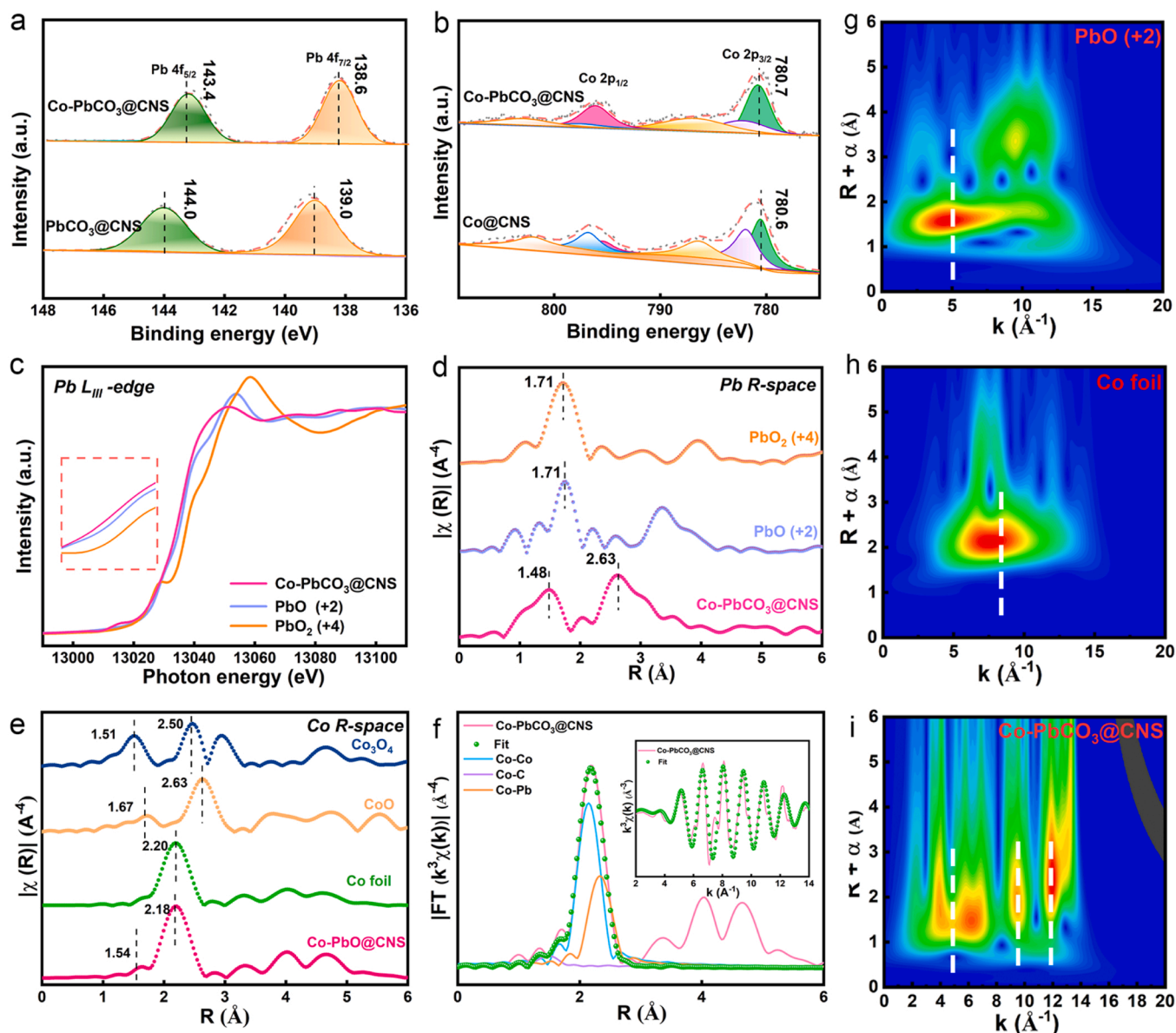
Fig. 3. XPS spectra of the (a) Pb 4 f and (b) Co 2p of Co-PbCO$_3$ @CNS and PbO@CNS or Co@CNS. (c) Pb L$_{III}$-edge XANES spectra, and (d) FT k$_3$-weighted EXAFS spectra for Pb L edge of Co-PbCO$_3$ @CNS and reference samples. (e)-(g) The Wavelet transform (WT) spectra of Co atoms in Co-PbCO$_3$ @CNS and reference samples.

crystallite size of ca. 16–26 nm (Fig. 1d). The atomic-resolution AC HAADF-STEM indicates a series of lattice fringes corresponding (marked with orange lines) to the (111) and (021) planes of PbCO$_3$ (Fig. 2a-b and e-f). The 2D lattice structure can be indexed to the PbCO$_3$ crystal structure viewed down the [111] and [021] zone axis. The filtered image shows that the lattice fringes of PbCO$_3$ are consecutive and clear (Fig. 2c and g). In addition, Fig. 2a and the EDS mapping images (Fig. 2d) displays a distinct interface about Co and PbCO$_3$, which was strong evidence for the successful construction of heterostructures. And the Fig. 2 h show that the Pb, Co, O and C elements distribute uniformly in the Co-PbCO$_3$ @CNS illustrating the uniform doping of Co in the Co-PbCO$_3$ @CNS and the images indicate that Pb and Co are highly overlapped [29]. In summary, Co doping in the Co-PbCO$_3$ @CNS exists two structural forms: heterojunction and uniform doping. The inductively coupled plasma-optical emission spectrometer (ICP-OES) test results show that the actual ratio of Co: Pb in Co-PbCO$_3$ @CNS sample is 0.09:1 (Fig. S5) indicates the content of Co-doping is low. The Raman spectrum of Co-PbCO$_3$ @CNS indicates the disordered carbon structure of carbon nanosheet (Fig. S6).

The surface valence states of Pb and Co were examined by X-ray photoelectron spectroscopy (XPS). Deconvolution of the Pb 4 f spectrum in PbCO$_3$ @CNS yields two main peak at 139.0 eV and 144.0 eV, which are attributable to the 4 f$_{7/2}$ and 4 f$_{5/2}$ electrons of Pb^{2+}, respectively (Fig. 3a) [19,30]. The Pb 4 f spectrum of Co-PbCO$_3$ @CNS (Fig. 3a) yield different degrees of negatively shift, leading to the accumulation of electrons on Pb^{2+}. Compared with Co@CNS, the Co 2p$_{3/2}$ spectrum of Co-PbCO$_3$ @CNS yield some positively shift (Fig. 3b), suggesting the Co provides electrons to Pb^{2+} species [31]. Therefore, the construction of Co doping in PbCO$_3$ permits the electron transfer to result in CA-Pb^{2+}, which might promote the adsorption of HCOO* intermediates to improve the CO$_2$RR selectivity [5,32].

The XANES spectroscopy of Pb L$_{III}$-edge and Co K-edge was further carried out to research the local electronic structure of Pb^{2+} and Co in Co-PbCO$_3$ @CNS. The Pb L$_{III}$-edge region of the XANES spectrum of Co-PbCO$_3$ @CNS is located left the PbO (+2) reference, implying the valence state of lead species on Co-PbO$_3$ @CNS is lower than + 2 (Fig. 3c). It might arise out of some Pb^{2+} in Co-PbCO$_3$ @CNS coordination with Co, O or C atoms. The Fourier-transformed (FT) k^3-weighted
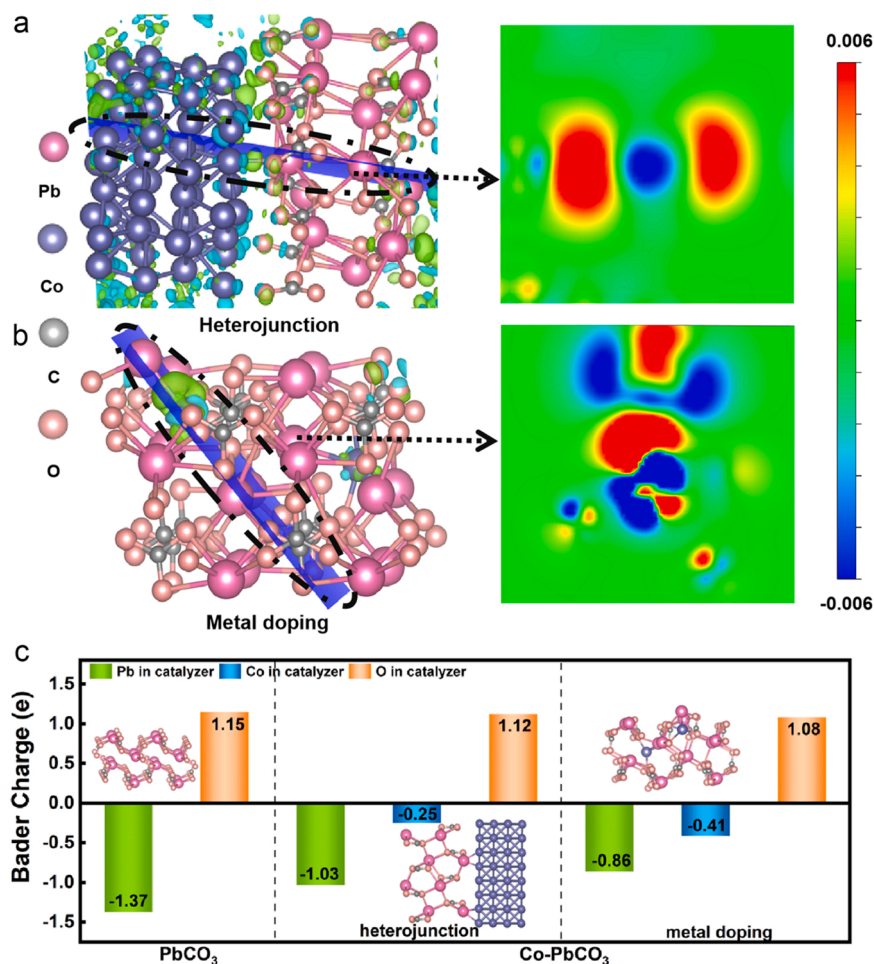
Fig. 4. (a) The charge density of Co-PbCO$_3$ heterojunction. (b) The charge density of metal-doped Co-PbCO$_3$. (c) The Bader charge analysis diagram of PbCO$_3$ and Co-PbCO$_3$ (heterojunction and metal doping).

EXAFS of Co-PbCO$_3$ @CNS displays peaks at around 1.48 Å and 2.63 Å. The peak of 2.63 Å is completely similar with PbO, which is assigned to the Pb-O bond.[10] The peak of 1.48 Å is preliminary suggested Co-Pb (Fig. 3d). The Fourier-transformed (FT) k^3-weighted EXAFS of Co-PbCO$_3$ @CNS in Fig. 3e displays two peaks at around 1.54 Å and 2.18 Å, respectively. The peak at 1.54 Å assigned to the coordination between cobalt and light elements such as carbon [33]. The peak of 2.18 Å was assigned to the Co-Co bond, moving 0.2 Å to the left compared with the Co-Co bonds of the Co foil. This further proved that a strong interaction between Co metal and PbO on the as prepared Co-PbO@CNS was formed. Moreover, Co-(O)-Co scattering paths of the reference CoO (2.63 Å) and Co$_3$O$_4$ (2.50 Å) were not observed in the Co-PbCO$_3$ @CNS, suggesting that CoOx species were almost absent on Co-PbCO$_3$ @CNS [33,34]. To give further insights into the coordination of Co in the sample of Co-PbCO$_3$ @CNS, the corresponding FT EXAFS fitting was conducted to extract the structural information. The Co$_2$C and CoPb$_3$ coordination moiety with 2.46 Å of Co-Co, 1.87 Å of Co-C and 2.71 Å of Co-Pb average bond lengths gave a reasonably good fit of the FT EXAFS spectrum of the as-prepared Co-PbCO$_3$ @CNS (Fig. 3f, Table S1). The wavelet transform (WT) analysis served to further substantiate this result. The intensity maximum of Co-PbCO$_3$ @CNS is at ca. 5.1 Å^{-1}, 9.3 Å^{-1} and 12.1 Å^{-1} (Fig. 3i). The 5.1 Å^{-1} is close to the reference PbO (5.0 Å^{-1}), representing the Pb-O (Fig. 3g). The intensity maximum of 12.1 Å^{-1} of Co-PbCO$_3$ @CNS shows a heavier metal coordination is Pb-Pb. The peak of 9.3 Å^{-1} is somewhere between Pb-Pb (12.1 Å^{-1}) and Co-Co (7.8 Å^{-1}), this could prove to be Pb-Co in theory. As indicated above, it is proved that the Co doping plays a role in

regulating the electronic environment of Pb^{2+}, leading the CA-Pb^{2+}.

The electron state of Pb active sites in Co-PbCO$_3$ was further investigated by DFT calculation, and models of Co-PbCO$_3$ (heterojunction and metal doping) and pure PbCO$_3$ were constructed (Fig. S26). There is an obvious electron transfer phenomenon in these two structures (the blue cross section in the left part), which demonstrate these parts of the charge of Co atom is transferred to Pb^{2+} (Fig. 4a-b). The Bader charge analysis reveals the charge numbers of cobalt in Co-PbCO$_3$ heterojunction and metal doping is − 0.25 eV and − 0.41 eV, respectively. And the charge number of Pb^{2+} in pure PbCO$_3$ (−1.37 eV) is more negative than that of Co-PbCO$_3$ in heterojunction (−1.03 eV) and metal doping (−0.86 eV) (Fig. 4c), revealing the charge of Co atom is transferred to Pb^{2+} in Co-PbCO$_3$, theoretically proves the obtain of CA-Pb^{2+}.

3.2. Electrochemical performances of Co-PbCO$_3$@CNS

The capability of Co-PbCO$_3$ @CNS in electrocatalytic CO$_2$RR was examined using a typical three-electrode setup in a H-type cell, and the operation process is displayed in the Supporting Information. As shown in Fig. 5a, the current density of Co-PbCO$_3$ @CNS acquired by the linear sweep voltammetry (LSV) curves are significantly higher than that in N$_2$-purged electrolyte, indicating apparent CO$_2$RR activity. After one hour of electrolysis, the liquid and gaseous products were analyzed to high performance liquid chromatography (HPLC), ^{1}H nuclear magnetic resonance (1 H NMR) spectroscopy and gas chromatography (GC) analyses, respectively. Remarkably, formate is the predominant product of CO$_2$RR, with a maximum of FE$_{formate}$ of 98.15% at − 0.70 V vs. RHE,
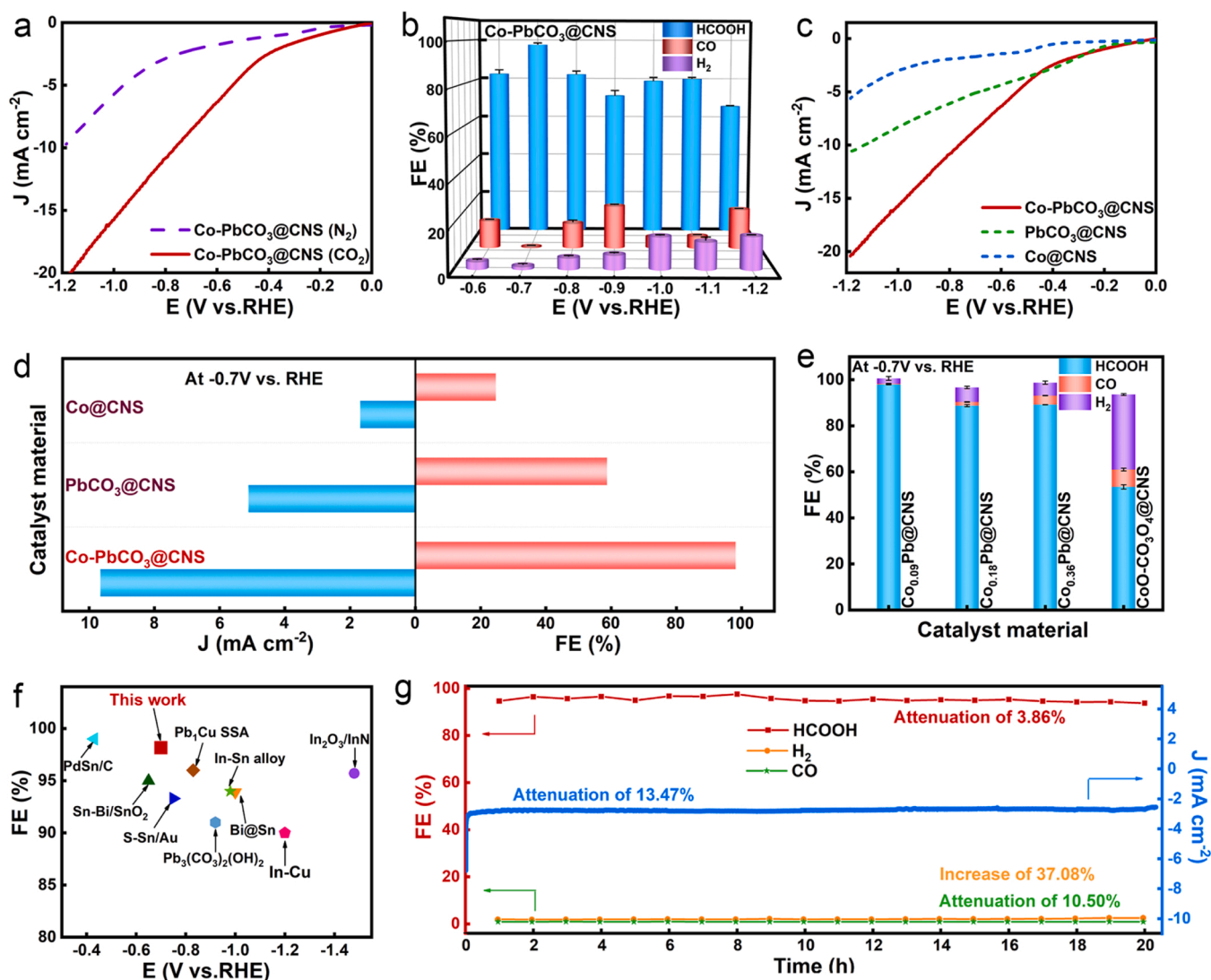
Fig. 5. (a) LSV curves of Co-PbCO$_3$ @CNS in N$_2$ and CO$_2$ (red line) saturated 0.1 M KHCO$_3$. (b) FE of formate, CO and H$_2$ on Co-PbCO$_3$ @CNS. (c) Partial current densities of formate on Co-PbCO$_3$ @CNS, PbCO$_3$ @CNS and Co@CNS. (d) The current density and FE$_{formate}$ about Co-PbCO$_3$ @CNS, PbCO$_3$ @CNS and Co@CNS. (e) The FE of formate, CO and H$_2$ on other Co-PbCO$_3$ @CNS samples with different Co:Pb ratio. (f) Comparison of FE$_{formate}$ of the catalysts reported in the literature. (g) Stability test of Co-PbCO$_3$ @CNS at − 0.70 V for 20 h, current density and FE$_{formate}$ stability.

whereas H$_2$ and CO account for only a very tiny portion of the final products (Fig. 5b and Fig. S7-S9). The Co-PbCO$_3$ @CNS has been demonstrated a strong selectivity for CO$_2$RR to formate. Fig. 5c shows the LSV curves of Co-PbCO$_3$ @CNS, PbCO$_3$ @CNS and Co@CNS tested in CO$_2$-saturated 0.1 M KHCO$_3$ electrolytic. Co-PbCO$_3$ @CNS shows a current density (21.52 mA cm^{-2}) that is higher than both PbCO$_3$ @CNS (10.87 mA cm^{-2}) and Co@CNS (5.62 mA cm^{-2}), and Co-PbCO$_3$ @CNS exhibits a low onset potential. These results demonstrate the remarkable activity of CO$_2$RR over the Co-PbCO$_3$ @CNS [35]. The FE for various products were examined over Co-PbCO$_3$ @CNS, PbCO$_3$ @CNS and Co@CNS catalysts at various voltages (Fig. 5d and S10). It can be seen that Co-PbCO$_3$ @CNS exhibits much higher FE$_{formate}$ than that of PbCO$_3$ @CNS and Co@CNS at all applied voltage. Specifically, the maximum FE$_{formate}$ over Co-PbCO$_3$ @CNS is 98.15% at − 0.70 V vs. RHE, which is significantly higher than the FE$_{formate}$ over pure PbCO$_3$ @CNS (58.74%) and Co@CNS (24.65%). Furthermore, the CNS substrate is essentially active for the generation of H$_2$ over the whole potential window, the combined FE of formate and CO is at most 2.5% (Fig. S11), suggesting that the Co-PbCO$_3$ on Co-PbCO$_3$ @CNS is the electroactive species for the generation of formate. Moreover, compared to pure PbCO$_3$ @CNS (5.11 mA cm^{-2}) and Co@CNS (1.69 mA cm^{-2}), Co-PbCO$_3$ @CNS

achieves a much higher formate partial current density (9.65 mA cm^{-2}), confirming the high catalytic activity in the CO$_2$RR to formate.

To determine the underlying causes for the enhanced CO$_2$RR performances of Co-PbCO$_3$ @CNS, double-layer capacitance measurements and electrochemical impedance spectroscopy (EIS) were performed (Fig. S12 and S13). In comparison to PbCO$_3$ @CNS and Co@CNS, the Co-PbCO$_3$ @CNS has a larger electrochemical surface area (ECSA) and a lower charge transfer resistance (Rct). The Tafel slope of Co-PbCO$_3$ @CNS is much lower (57.83 mV dec^{-1}) than that of the two compared samples, which is in favor of the improvement of kinetic activity (Fig. S14). Moreover, other Co-PbCO$_3$ @CNS samples with different Co: Pb ratio (0.18:1, 0.36:1 and 0.90:1) were also prepared (Fig. S15 and S16). The Co-PbCO$_3$ @CNS with the actual Co:Pb ratio of 0.09:1 shows the largest current density (Fig. S17) and the best selectivity for formate (Fig. 5e and S18). Compared with related catalysts reported in the literature, the Co-PbCO$_3$ @CNS displays a excellent selectivity for CO$_2$RR to formate at − 0.70 V vs RHE (Fig. 5f) [1,9,10,22,35–39]. Additionally, in 0.1 M KHCO$_3$ electrolyte, the FE$_{formate}$ and current density on Co-PbCO$_3$ @CNS is practically unchanged at − 0.70 V for 20 h (Fig. 5g). The Co-PbCO$_3$ @CNS after testing can still remain typical nanosheet morphology (Fig. S19), the XRD, XPS and AC HAADF-STEM
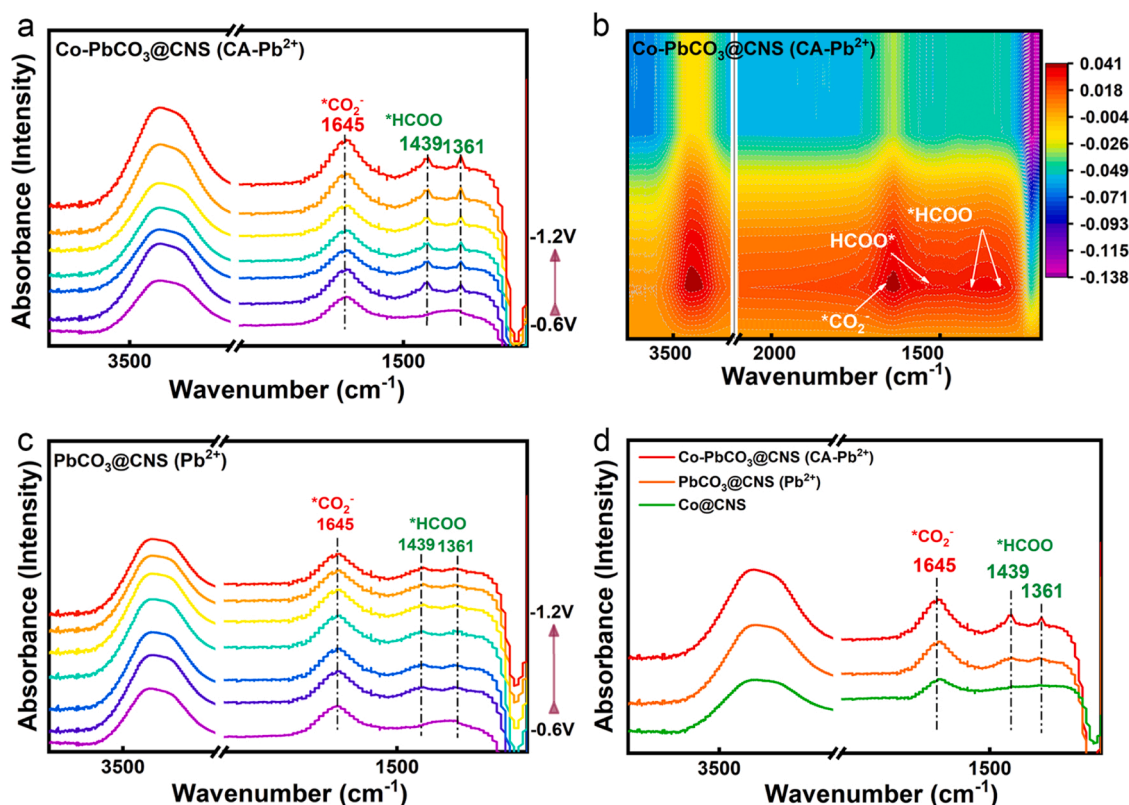
Fig. 6. (a)-(b) In-situ ATR-SEIRAS spectra of Co-PbCO$_3$ @CNS in CO$_2$-saturated 0.1 M KHCO$_3$ solution from − 0.60 V to − 1.20 V vs. RHE. (c) In-situ ATR-SEIRAS spectra of PbCO$_3$ @CNS in CO$_2$-saturated 0.1 M KHCO$_3$ solution from − 0.60 V to − 1.20 V vs. RHE. (d) In-situ ATR-SEIRAS spectra of Co-PbCO$_3$ @CNS, PbCO$_3$ @CNS and Co@CNS in CO$_2$-saturated 0.1 M KHCO$_3$ solution at − 0.70 V vs. RHE.

indicate the structures of Co-PbCO$_3$ @CNS before and after the stability test are nearly identical, which indicate that the structural stability of Co-PbCO$_3$ @CNS (Fig. S20-S22). In summary, Co-PbCO$_3$ @CNS is one of the catalytic with excellent stability. In addition, inductively coupled plasma mass spectrometry (ICP-MS) was used to determine the leaching of lead and cobalt ions after 20 h test, and the leaching amount of Co^{2+} and Pb^{2+} are only 0.024 mg L^{-1} and 0.058 mg L^{-1} (Fig. S23), which proves that the Co-PbCO$_3$ @CNS has the potential of long cycle stability. In order to identify the electrolyte effects on performance, the different cations and concentrations of electrolytes were used to test performance. The CO$_2$RR performance was affected by the metal cation employed and the obtained FE$_{formate}$ was in the order of K$^+$ > Na$^+$, and the different electrolyte concentration has little effect on the performance of these materials (Fig. S24).

3.3. The ATR-SEIRAS

To reveal the reaction mechanism and active site of CO$_2$RR to fomate over Co-PbCO$_3$ @CNS (CA-Pb^{2+}), PbCO$_3$ @CNS (Pb^{2+}) and Co@CNS catalysts, the ATR-SEIRAS was carried out in CO$_2$-saturated KHCO$_3$ solution at − 0.60 V to − 1.20 V vs. RHE. For Co-PbCO$_3$ @CNS, the peaks of *CO$_2$ at 1645 cm^{-1} are ascribed to the activation of CO$_2$ molecules on Co-PbCO$_3$ @CNS catalyst surface (Fig. 6a and b) [8,40]. The characteristic peaks at 1361 and 1439 cm^{-1} are caused by the asymmetric stretching vibration of O-C-O, which indicate the formation of *HCOO pathway on CA-Pb^{2+} [41]. This pathway first appeared at − 0.70 V vs. RHE and subsequently expanded with the increasing of applied potentials [8,9,42,43]. The presence of *CO$_2$, HCOO* are the key intermediate for the formate product [44]. However, the ATR-SEIRAS peak of Co@CNS is only assigned to the *CO$_2$, meaning the little potential of CO$_2$ to formate (Fig. S25). For PbCO$_3$ @CNS, it has a similar trend and peak position to Co-PbCO$_3$ @CNS, also indicates the reaction pathways by

which formate is formed (Fig. 6c). Notably, over Co-PbCO$_3$ @CNS at − 0.7 V vs. RHE, the intensity of the HCOO* intermediate is higher than that of PbCO$_3$ @CNS (Fig. 6d). This indicates the CA-Pb^{2+} can encourage the activation of CO$_2$ and further generate and adsorb the HCOO* to improve the activity and selectivity of formate product.

3.4. DFT calculations

The Gibbs free energies (ΔG) of CO$_2$RR to formate on CA-Pb^{2+} (heterojunction and metal uniform doping) and Pb^{2+} in models by DFT calculation were constructed and presented to unravel the energetics and reaction pathways (Fig. 7a-g and S27) [45]. The HCOO* is an important intermediate for formate production. In this pathway, the ΔG of HCOO* formation (ΔG$_{HCOO*}$) of CA-Pb^{2+} heterojunction (−0.78 eV) and CA-Pb^{2+} of metal doping (−1.01 eV) are much lower than that of Pb^{2+} (1.16 eV), indicating the electron-rich CA-Pb^{2+} sites of heterojunction and metal doping act synergistically in inducing the reduced formation energy barrier of HCOO* intermediate. The ΔG of H* adsorption on CA-Pb^{2+} (0.50 eV and 1.48 eV) is markedly bigger than the ΔG$_{HCOO*}$, which the competing hydrogen evolution reaction is inhibited (Fig. S28). Moreover, the ΔG of *COOH formation (ΔG$_{COOH*}$ = 0.34 eV) in CA-Pb^{2+} heterojunction and ΔG$_{COOH*}$ = 0.114 eV in metal doping-CA-Pb^{2+} are all higher than ΔG$_{HCOO*}$, which confirms the effective hindrance in the *COOH formation process (Fig. 7 h and S29).

The ATR-SEIRAS and DFT calculation results prove that the CA-Pb^{2+} active sites modified by Co facilitates the formation and adsorption of the key HCOO* intermediate to induce highly active and selective CO$_2$RR to formate.

4. Conclusions

In summary, the Co modified PbCO$_3$ loaded carbon nanosheet
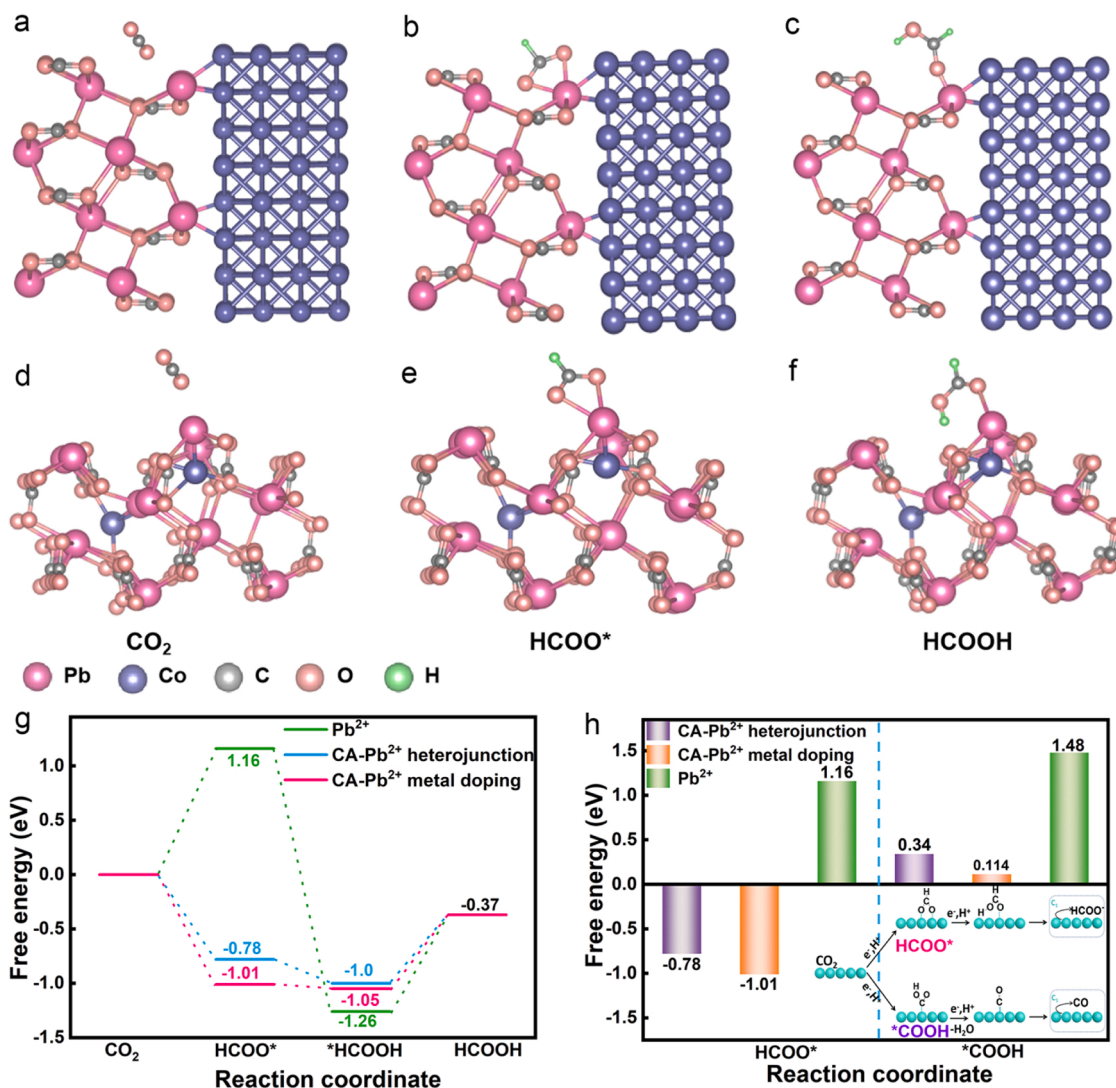
Fig. 7. (a)-(c) Adsorption configurations of CO_2, HCOO* and HCOOH on Co-PbCO$_3$ of heterojunction and (d)-(f) metal uniform doping (pink for Pb, blue for Co, gray for C, yellow for O and green for H in reaction intermediates). (g) Free energy diagrams of CO_2RR to formate on Pb in CA-Pb^{2+} and PbCO$_3$ @CNS. (h) Free energy diagrams in CO_2RR for formation of HCOO* and *COOH on Pb in CA-Pb^{2+} and Pb^{2+}.

electrocatalyst for CO_2RR to formate was synthesized and exhibited highly catalytic activity, selectivity and stability. The Co-Pb^{2+} interaction in Co modified Pb^{2+} structure stimulates the electron transfer to lead charge-acquired-Pb^{2+}. Such electron-rich Pb^{2+} sites induce the lower formation energy barrier and preferential adsorption of HCOO*- intermediate to pure Pb^{2+} sites, verifying their highly catalytic activity and selectivity of CO_2RR to formate. This work demonstrates the significance of electronic structural regulation in manipulating and optimizing the lead-based electrocatalysts for highly selective CO_2RR to formate. Such fundamental insights may be exploited for optimizing the environmentally functional electrocatalysts to promote the electrochemical energy and matter conversion.

CRediT authorship contribution statement

Ningce Zhang and Daohao Li designed and performed the experiments. Xiaoxia Wang performed the theoretical calculations. Ningce Zhang performed part experiments and characterization. Rongsheng Cai conducted aberration-corrected high-resolution transmission electron microscope measurement. ChungLi Dong and Ta Thi Thuy Nga performed X-ray adsorption measurement. Ningce Zhang, Daohao Li, Lijie Zhang and Dongjiang Yang wrote the manuscript with input from all authors. All authors discussed the obtained results.

Declaration of Competing Interest

The authors declare that they have no known competing financial interests or personal relationships that could have appeared to influence the work reported in this paper.

Data Availability

Data will be made available on request.

Acknowledgments

Appendix A. Supporting information

Supplementary data associated with this article can be found in the online version at doi:10.1016/j.apcatb.2023.122404.

References

[1] J. Wang, S. Ning, M. Luo, D. Xiang, W. Chen, X. Kang, Z. Jiang, S. Chen, In-Sn alloy core-shell nanoparticles: in-doped SnO_x shell enables high stability and activity towards selective formate production from electrochemical reduction of CO_2, Appl. Catal. B Environ. 288 (2021), 119979.

[2] X. Zhang, Z. Chen, M. Jiao, X. Ma, K. Mou, F. Cheng, Z. Wang, X. Zhang, L. Liu, Defects and conductive nitrogen-carbon framework regulated $ZnInO_x$ nanosheets for boosting CO_2 electrocatalytic reduction, Appl. Catal. B Environ. 279 (2020), 119383.

[3] S.-G. Han, D.-D. Ma, S.-H. Zhou, K. Zhang, W.-B. Wei, Y. Du, X.-T. Wu, Q. Xu, R. Zou, Q.-L. Zhu, Fluorine-tuned single-atom catalysts with dense surface $Ni-N_4$ sites on ultrathin carbon nanosheets for efficient CO_2 electroreduction, Appl. Catal. B Environ. 283 (2021) 119591.

[4] N. Han, Y. Wang, H. Yang, J. Deng, J. Wu, Y. Li, Y. Li, Ultrathin bismuth nanosheets from in situ topotactic transformation for selective electrocatalytic CO_2 reduction to formate, Nat. Commun. 9 (2018) 1320.

[5] J. Gu, C.-S. Hsu, L. Bai, H.M. Chen, X. Hu, Atomically dispersed Fe^{3+} sites catalyze efficient CO_2 electroreduction to CO, Science 364 (2019) 1091–1094.

[6] Y. Xing, X. Kong, X. Guo, Y. Liu, Q. Li, Y. Zhang, Y. Sheng, X. Yang, Z. Geng, J. Zeng, Bi@Sn core-shell structure with compressive strain boosts the electroreduction of CO_2 into formic acid, Adv. Sci. 7 (2020), 1902989.

[7] P. Lu, X. Tan, H. Zhao, Q. Xiang, K. Liu, X. Zhao, X. Yin, X. Li, X. Hai, S. Xi, A.T. S. Wee, S.J. Pennycook, X. Yu, M. Yuan, J. Wu, G. Zhang, S.C. Smith, Z. Yin, Atomically dispersed indium sites for selective CO_2 electroreduction to formic acid, ACS Nano 15 (2021) 5671–5678.

[8] W. Xie, H. Li, G. Cui, J. Li, Y. Song, S. Li, X. Zhang, J.Y. Lee, M. Shao, M. Wei, NiSn atomic pair on an integrated electrode for synergistic electrocatalytic CO_2 reduction, Angew. Chem. Int. Ed. 60 (2021) 7382–7388.

[9] Z. Wu, H. Wu, W. Cai, Z. Wen, B. Jia, L. Wang, W. Jin, T. Ma, Engineering bismuth-tin interface in bimetallic aerogel with a 3D porous structure for highly selective electrocatalytic CO_2 reduction to HCOOH, Angew. Chem. Int. Ed. 60 (2021) 12554–12559.

[10] Y. Shi, Y. Ji, J. Long, Y. Liang, Y. Liu, Y. Yu, J. Xiao, B. Zhang, Unveiling hydrocerussite as an electrochemically stable active phase for efficient carbon dioxide electroreduction to formate, Nat. Commun. 11 (2020) 3415.

[11] H. Wang, Z. Liang, M. Tang, G. Chen, Y. Li, W. Chen, D. Lin, Z. Zhang, G. Zhou, J. Li, Z. Lu, K. Chan, T. Tan, Y. Cui, Self-selective catalyst synthesis for CO_2 reduction, Joule 3 (2019) 1927–1936.

[12] M. Alvarez-Guerra, S. Quintanilla, A. Irabien, Conversion of carbon dioxide into formate using a continuous electrochemical reduction process in a lead cathode, Chem. Eng. J. 207–208 (2012) 278–284.

[13] L. Chen, F. Li, C.L. Bentley, M. Horne, A.M. Bond, J. Zhang, Electrochemical reduction of CO_2 with an oxide-derived lead nano-coralline electrode in dimcarb, ChemElectroChem 4 (2017) 1402–1410.

[14] Q. Zhu, J. Ma, X. Kang, X. Sun, H. Liu, J. Hu, Z. Liu, B. Han, Efficient reduction of CO_2 into formic acid on a lead or tin electrode using an ionic liquid catholyte mixture, Angew. Chem. Int. Ed. 55 (2016) 9012–9016.

[15] Z. He, J. Shen, Z. Ni, J. Tang, S. Song, J. Chen, L. Zhao, Electrochemically created roughened lead plate for electrochemical reduction of aqueous CO_2, Catal. Commun. (2015) 5.

[16] A.M. Ismail, G.F. Samu, H.C. Nguyễn, E. Csapó, N. López, C. Janáky, Au/Pb interface allows the methane formation pathway in carbon dioxide electroreduction, ACS Catal. (2020) 10.

[17] C.H. Lee, M.W. Kanan, Controlling H^+ vs CO_2 reduction selectivity on Pb electrodes, ACS Catal. 5 (2015) 465–469.

[18] Z. Wang, H.-F. Su, L.-P. Zhang, J.-M. Dou, C.-H. Tung, D. Sun, L. Zheng, Stepwise assembly of Ag_{42} nanocalices based on a Mo^{VI}-anchored thiacalix [4] arene Metalloligand, ACS Nano 16 (2022) 4500–4507.

[19] S.Y. Choi, S.K. Jeong, H.J. Kim, I.-H. Baek, K.T. Park, Electrochemical reduction of carbon dioxide to formate on tin-lead alloys, ACS Sustain. Chem. Eng. 4 (2016) 1311–1318.

[20] A. Hailu, A.A. Tamijani, S.E. Mason, S.K. Shaw, Efficient conversion of CO_2 to formate using inexpensive and easily prepared post-transition metal alloy catalysts, Energy Fuels 34 (2020) 3467–3476.

[21] Y. Wang, H. Hu, Y. Sun, Y. Tang, L. Dai, Q. Hu, A. Fisher, X.J. Yang, Facile synthesis of nanostructural high-performance Cu-Pb electrocatalysts for CO_2 reduction, Adv. Mater. Interfaces 6 (2019), 1801200.

[22] T. Zheng, C. Liu, C. Guo, M. Zhang, X. Li, Q. Jiang, W. Xue, H. Li, A. Li, C.-W. Pao, J. Xiao, C. Xia, J. Zeng, Copper-catalysed exclusive CO_2 to pure formic acid conversion via single-atom alloying, Nat. Nanotechnol. 16 (2021) 1386–1393.

[23] A.S. Kumawat, A. Sarkar, Comparative study of carbon supported Pb, Bi and Sn catalysts for electroreduction of carbon dioxide in alkaline medium, J. Electrochem. Soc. 164 (2017) H1112–H1120.

[24] Y. Cheng, P. Hou, H. Pan, H. Shi, P. Kang, Selective electrocatalytic reduction of carbon dioxide to oxalate by lead tin oxides with low overpotential, Appl. Catal. B Environ. 272 (2020), 118954.

[25] J. Wu, X. Bai, Z. Ren, S. Du, Z. Song, L. Zhao, B. Liu, G. Wang, H. Fu, Multivalent Sn species synergistically favours the CO_2-into-HCOOH conversion, Nano Res 14 (2021) 1053–1060.

[26] Z. Zhang, Z. Wen, D. Luo, B. Ren, Y. Zhu, R. Gao, H. Dou, G. Sun, M. Feng, Z. Bai, A. Yu, Z. Chen, Two ships in a bottle" design for Zn-Ag-O catalyst enabling selective and long-lasting CO_2 electroreduction, J. Am. Chem. Soc. 143 (2021) 6855–6864.

[27] H. Li, X. Zhao, H. Liu, S. Chen, X. Yang, C. Lv, H. Zhang, X. She, D. Yang, Sub-1.5 nm ultrathin CoP nanosheet aerogel: efficient electrocatalyst for hydrogen evolution reaction at all pH values, Small 14 (2018), 1802824.

[28] Y. Zou, Q. Chang, S. Chen, T. Liu, Y. Xia, C. Chen, D. Yang, Alginate/r-GO assisted synthesis of ultrathin $LiFePO_4$ nanosheets with oriented (010) facet and ultralow antisite defect, Chem. Eng. J. 351 (2018) 340–347.

[29] C. Tang, X. Shen, X. Wu, Y. Zhong, J. Hu, M. Lu, Z. Wu, Y. Zhang, W.W. Yu, X. Bai, Optimizing the performance of perovskite nanocrystal LEDs utilizing cobalt doping on a ZnO electron transport layer, J. Phys. Chem. Lett. 12 (2021) 10112–10119.

[30] N. Zouaoui, B.D. Ossonon, M. Fan, D. Mayilukila, S. Garbarino, G. de Silveira, G. A. Botton, D. Guay, A.C. Tavares, Electroreduction of CO_2 to formate on amine modified Pb electrodes, J. Mater. Chem. A. 7 (2019) 11272–11281.

[31] L. Zhang, T. Liu, N. Chen, Y. Jia, R. Cai, W. Theis, X. Yang, Y. Xia, D. Yang, X. Yao, Scalable and controllable synthesis of atomic metal electrocatalysts assisted by an egg-box in alginate, J. Mater. Chem. A 6 (2018) 18417–18425.

[32] Z. Chen, G. Zhang, Y. Wen, N. Chen, W. Chen, T. Regier, J. Dynes, Y. Zheng, S. Sun, Atomically dispersed Fe-Co bimetallic catalysts for the promoted electroreduction of carbon dioxide, Nano-Micro Lett. 14 (2022) 25.

[33] M. Ma, J. Chen, Z. Huang, W. Fa, F. Wang, Y. Cao, Y. Yang, Z. Rao, R. Wang, R. Zhang, Y. Zou, Y. Zhou, Intermolecular hydrogen bond modulating the selective coupling of protons and CO_2 to CH_4 over nitrogen-doped carbon layers modified cobalt, Chem. Eng. J. 444 (2022), 136585.

[34] M. Ma, Z. Huang, D.E. Doronkin, W. Fa, Z. Rao, Y. Zou, R. Wang, Y. Zhong, Y. Cao, R. Zhang, Y. Zhou, Ultrahigh surface density of $Co-N_2C$ single-atom-sites for boosting photocatalytic CO_2 reduction to methanol, Appl. Catal. B Environ. 300 (2022), 120695.

[35] X. Zhao, M. Huang, B. Deng, K. Li, F. Li, F. Dong, Interfacial engineering of In_2O_3/InN heterostructure with promoted charge transfer for highly efficient CO_2 reduction to formate, Chem. Eng. J. 437 (2022), 135114.

[36] X. Bai, W. Chen, C. Zhao, S. Li, Y. Song, R. Ge, W. Wei, Y. Sun, Exclusive formation of formic acid from CO_2 electroreduction by a tunable Pd-Sn alloy, Angew. Chem. Int. Ed. 56 (2017) 12219–12223.

[37] L. Li, A. Ozden, S. Guo, F.P. García de Arquer, C. Wang, M. Zhang, J. Zhang, H. Jiang, W. Wang, H. Dong, D. Sinton, E.H. Sargent, M. Zhong, Stable, active CO_2 reduction to formate via redox-modulated stabilization of active sites, Nat. Commun. 12 (2021) 5223.

[38] V.C. Hoang, V.G. Gomes, N. Kornienko, Metal-based nanomaterials for efficient CO_2 electroreduction: recent advances in mechanism, material design and selectivity, Nano Energy 78 (2020), 105311.

[39] B. Wei, Y. Xiong, Z. Zhang, J. Hao, L. Li, W. Shi, Efficient electrocatalytic reduction of CO_2 to HCOOH by bimetallic In-Cu nanoparticles with controlled growth facet, Appl. Catal. B Environ. 283 (2021) 119646.

[40] Y. Wang, J. Zhao, T. Wang, Y. Li, X. Li, J. Yin, C. Wang, CO_2 photoreduction with H_2O vapor on highly dispersed CeO_2/TiO_2 catalysts: Surface species and their reactivity, J. Catal. 337 (2016) 293–302.

[41] B. Innocent, D. Pasquier, F. Ropital, F. Hahn, J.-M. Léger, K.B. Kokoh, FTIR spectroscopy study of the reduction of carbon dioxide on lead electrode in aqueous medium, Appl. Catal. B Environ. 94 (2010) 219–224.

[42] J. Di, P. Song, C. Zhu, C. Chen, J. Xiong, M. Duan, R. Long, W. Zhou, M. Xu, L. Kang, B. Lin, D. Liu, S. Chen, C. Liu, H. Li, Y. Zhao, S. Li, Q. Yan, L. Song, Z. Liu, Strain-engineering of $Bi_{12}O_{17}Br_2$ nanotubes for boosting photocatalytic CO_2 reduction, ACS Mater. Lett. 2 (2020) 1025–1032.

[43] M. Wang, M. Shen, X. Jin, J. Tian, M. Li, Y. Zhou, L. Zhang, Y. Li, J. Shi, Oxygen vacancy generation and stabilization in CeO_{2-x} by Cu introduction with improved CO_2 photocatalytic reduction activity, ACS Catal. 9 (2019) 4573–4581.

[44] X. Cao, D. Tan, B. Wulan, K.S. Hui, K.N. Hui, J. Zhang, In situ characterization for boosting electrocatalytic carbon dioxide reduction, Small Methods 5 (2021), 2100700.

[45] A.A. Peterson, J.K. Nørskov, Activity descriptors for CO_2 electroreduction to methane on transition-metal catalysts, J. Phys. Chem. Lett. 3 (2012) 251–258.